

# Rayleigh surface waves and phonon mode conversion in nanostructures

L. N. Maurer\* and I. Knezevic†

*University of Wisconsin-Madison, Madison, Wisconsin 53706, USA*

(Dated: 2022/06/25)

We study the effects of phonon mode conversion and Rayleigh (surface) waves on thermal transport in nanostructures. We present a technique to calculate thermal conductivity in the elastic-solid approximation: a finite-difference time-domain (FDTD) solution of the elastic or scalar wave equations combined with the Green-Kubo formula. The technique captures phonon wave behavior and scales well to nanostructures that are too large or too surface disordered to simulate with many other techniques. By imposing fixed or free boundary conditions, we can selectively turn off mode conversion and Rayleigh waves to study their effects. In the example case of graphenelike nanoribbons, we find that mode conversion among bulk modes has little effect on thermal transport, but that conversion between bulk and Rayleigh waves can drastically reduce thermal conductivity. With increasing surface disorder, Rayleigh waves readily localize and draw energy away from the propagating bulk modes, which lowers thermal conductivity. We discuss the implications on the accuracy of popular phonon-surface scattering models that stem from scalar wave equations and cannot capture mode conversion to Rayleigh waves.

PACS numbers: 66.70.-f, 63.22.-m, 62.30.+d, 68.65.-k, 68.35.Ja

## I. INTRODUCTION

Phonon-surface scattering is inherently a multi-phonon process. In general, a single phonon scattering from a surface will be split into multiple outgoing phonons of different modes, a phenomenon known as mode conversion [1–4]. At smooth surfaces, bulk phonons (longitudinal and transverse) can be converted only to other bulk phonons [1, 5]. Structures with free surfaces support Rayleigh surface waves (Fig. 1) [1, 6–8], so bulk modes can also convert to Rayleigh waves at rough [9, 10] or otherwise disordered [3, 11, 12] free surfaces. Rayleigh waves travel slower than bulk modes [1] and have relatively long lifetimes even in the presence of disorder [11, 13].

Understanding Rayleigh waves is important for modeling thermal transport in modern nanostructures [14–17], because Rayleigh waves concentrate energy near the surface, where disorder is often high [18–20]. Yet, relatively little is known about the effects of Rayleigh waves and surface modes in general on phonon thermal transport. Early work on Rayleigh waves focused on their decay into bulk waves in the presence of disorder [9, 11, 12, 21, 22], but did not address phonon transport. In spite of considerable recent interest in phonon transport at the nanoscale [14], surface modes in disordered nanostructures have received limited attention. Nakayama [3] identified Rayleigh wave mode conversion as a cause of diffuse surface scattering, which is important to many phonon-surface scattering models [23–25]. Kang and Estreicher [26] used a molecular dynamics simulation to show that mode conversion between bulk modes and localized surface modes can lead to “phonon trapping,” which can greatly reduce thermal conductivity. Maznev

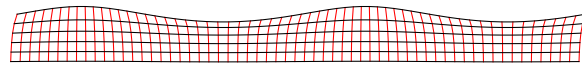


FIG. 1. (Color online) Illustration of a Rayleigh wave propagating along the free top surface. The wave amplitude decays exponentially with increasing distance from the surface.

[10] investigated elastic wave scattering from a nearly smooth surface using a Green’s function technique and found that a majority of the energy from a normally incident longitudinal wave can undergo mode conversion into Rayleigh waves, but mode conversion at other angles was not addressed. Mode conversion has been examined in superlattices, both experimentally [27] and theoretically, by treating the superlattices as continuum materials [28–30].

Elastic continuum materials are excellent model systems for studying the effects of phonon-surface scattering, mode conversion, and Rayleigh waves. Elastic materials are a simpler, long-wavelength limit of atomic materials [31] and they support acoustic longitudinal, acoustic transverse, Rayleigh, [1, 7, 8] and structure-dependent modes (such as torsional modes for a wire [32]). The study of elastic continuum materials can provide important insights into phonon-surface scattering in atomic materials [10, 33–36], especially for long-wavelength modes in the nanostructures that are too large to treat directly using atomistic techniques, yet too small to be considered bulk [14–17].

In this paper, we examine the effects of mode conversion and Rayleigh waves on thermal conductivity in nanostructures with surface disorder. We simulate two-dimensional (2D) graphenelike nanoribbons with random, rough edges using both elastic and scalar waves with free and fixed boundary conditions (BCs). These combinations of wave equations and BCs let us selectively “turn off” Rayleigh waves and mode conversion to study

\* lnmaurer@wisc.edu

† irena.knezevic@wisc.edu

their effects. We solve both the elastic and scalar wave equations with the finite-difference time-domain (FDTD) technique, which is efficient and not limited to weak roughness. We couple the FDTD simulation with the Green-Kubo formula to calculate the thermal conductivity. The combination of FDTD and Green-Kubo has similarities to an equilibrium molecular dynamics (MD) simulation [37, 38], but scales better than MD as the system size increases and enables us to simulate large nanostructures with pronounced roughness. We find that mode conversion between bulk modes has a minor effect on heat conduction, but that conversion between bulk and Rayleigh waves dramatically reduces thermal conductivity. As the roughness is increased, the Rayleigh waves become localized, trapping energy and further reducing thermal conductivity. We consider the consequences for other phonon-surface scattering models, many of which do not include Rayleigh waves.

In Sec. II, we review the theory of elastic waves. We include subsections on the elastic wave and scalar wave equations (II A), physically relevant boundary conditions (II B), and an overview of Rayleigh waves (II C). In Sec. III, we introduce the FDTD simulation technique and the structures we simulate (III A) and explain how the method can be used with the Green-Kubo formula to compute thermal conductivity (III B). Based on the FDTD simulation, we illustrate how the interplay of the boundary conditions (free or fixed) with surface roughness affects the mode conversion channels and energy trapping near the surface (IV). In Sec. V, we report the calculated thermal conductivities for elastic and scalar wave equations with different types of boundary conditions. We demonstrate that Rayleigh waves siphon energy from inside the nanostructure and trap it near the surface, thereby lowering thermal conductivity. We conclude with Sec. VI by discussing the implications of Rayleigh waves and mode conversion on common phonon-surface scattering models.

## II. THEORETICAL FRAMEWORK

### A. Elastic and scalar wave equations

We consider isotropic, homogeneous, linearly elastic, continuum materials.  $\mathbf{u}(\mathbf{r}, t)$  is the displacement of an infinitesimal element of the material. The strain tensor

$$\sigma_{ij} = \frac{1}{2} (\partial_j u_i + \partial_i u_j) \quad (1a)$$

and the stress tensor  $\tau_{ij}$  are related by the continuum generalization of Hooke's law

$$\tau_{ij} = \lambda \sigma_{ll} \delta_{ij} + 2\mu \sigma_{ij}, \quad (1b)$$

where  $\lambda$  and  $\mu$  are the Lamé parameters, which are material dependent.  $\mu$  is also known as the shear modulus

and  $\mu > 0$ . Thermodynamic stability requires  $\lambda > -\frac{2}{3}\mu$  [1], but  $\lambda > 0$  for most materials [22].

The power flux for the elastic wave equation is

$$\mathbf{J} = -\boldsymbol{\tau} \cdot \dot{\mathbf{u}}. \quad (2)$$

$\mathbf{J}$  is the elastic wave equivalent of the Poynting vector for electromagnetic waves [5, 39]. In the context of thermal transport,  $\mathbf{J}$  is often called the heat flux.

Applying Newton's second law to the stress-strain relations yields the elastic wave equation

$$\begin{aligned} \rho \ddot{\mathbf{u}} &= \nabla \cdot \boldsymbol{\tau} \\ &= (\lambda + 2\mu) \nabla (\nabla \cdot \mathbf{u}) - \mu \nabla \times (\nabla \times \mathbf{u}), \end{aligned} \quad (3)$$

where  $\rho$  is the density.

By Helmholtz's theorem,  $\mathbf{u}$  can be written in terms of a scalar potential  $\phi$  and a vector potential  $\boldsymbol{\Psi}$

$$\mathbf{u} = \nabla \phi + \nabla \times \boldsymbol{\Psi}, \quad (4)$$

which allows us to split the elastic wave equation (3) into two scalar wave equations, one for longitudinal and one for transverse waves:

$$\nabla^2 \phi - \frac{1}{c_l^2} \ddot{\phi} = 0, \quad (5a)$$

$$\nabla^2 \boldsymbol{\Psi} - \frac{1}{c_t^2} \ddot{\boldsymbol{\Psi}} = 0, \quad (5b)$$

where  $c_l = \sqrt{\frac{\lambda+2\mu}{\rho}}$  and  $c_t = \sqrt{\frac{\mu}{\rho}}$  are the longitudinal and transverse wave speeds, respectively.

We consider nanoribbonlike, planar structures, so  $\boldsymbol{\Psi}$  will always be normal to the plane and can thus be treated as a scalar, since it has only one nonzero component. In other words, the elastic wave equation in 2D can be decomposed into two scalar wave equations that are decoupled inside the bulk. We do not explicitly consider out-of-plane modes in this paper; however, out-of-plane modes also follow the scalar wave equation and our scalar wave results could be generalized to out-of-plane modes.

As the elastic wave equation in the bulk can be decomposed into two simpler scalar wave equations, scalar waves are also used more often than elastic waves to model phonon-surface scattering [40–51]. However, the decomposition (4) into scalar waves generally does not hold near surfaces; as a result, the use of scalar waves to describe lattice-wave interactions with surfaces cannot capture the important phenomenon of mode conversion. Additionally, scalar waves cannot be used to model Rayleigh surface waves (see Sec. II C) or many structure-dependent waves [52].

### B. Boundary conditions

At the surface, we consider both fixed (Dirichlet) and free (Neumann) boundary conditions (BCs). Let  $\hat{n}$  be

the surface normal vector. For elastic waves, the fixed BC is  $\mathbf{u} = 0$  and the free BC is  $\tau\hat{n} = 0$ . For scalar waves, the fixed BC is  $\phi = 0$  and the free BC is  $\nabla\phi \cdot \hat{n} = 0$ .

Free-standing nanostructures (such as suspended graphene nanoribbons) have unrestrained surfaces, which are equivalent to free BCs. We also analyze fixed BCs, because fixing the boundaries enables us to “turn off” Rayleigh waves, which exist only for elastic waves near a free surface. Studying fixed BCs is also useful for understanding the nanostructures with edges that are not free, such as in supported graphene nanoribbons.

### C. Rayleigh waves

There are many types of surface waves in atomic and inhomogeneous elastic materials [7, 8, 22]. However, for the uniform elastic materials we consider, Rayleigh waves (Fig. 1) are the only type of surface wave [22]. Here, we briefly review some important facts about Rayleigh waves [1, 6].

The general form for a Rayleigh wave propagating in the  $x$ -direction near the surface of a semi-infinite bulk material ( $y \geq 0$ ) is given by

$$\mathbf{u}(x, y, t) = e^{i(kx - \omega t)} \left[ (a\gamma_t e^{-\gamma_t y} + bke^{-\gamma_l y}) \hat{\mathbf{x}} - i(ake^{-\gamma_t y} + b\gamma_l e^{-\gamma_l y}) \hat{\mathbf{y}} \right], \quad (6)$$

where  $k$  is the wave number,  $\omega$  is the angular frequency,  $a$  and  $b$  capture the amplitude of the wave at the surface, and  $\gamma_l$  and  $\gamma_t$  capture the exponential decay of amplitude away from the surface.

Rayleigh waves have a linear dispersion relation,  $\omega = c_r k$ , where  $c_r$  is the Rayleigh-wave group velocity.  $c_r$  has a complicated dependence on the Lamé parameters. For  $\lambda > 0$ ,  $0.874c_t < c_r < 0.955c_t$ . For the graphene-like Lamé parameters we use here (see Sec. III A),  $c_r = 0.89c_t$ ,  $\kappa_l = 2.19k$ ,  $\kappa_t = 3.85k$ , and  $a = 1.32b$ .

Rayleigh waves are slower than transverse or longitudinal waves, extend into the structure a distance comparable to their wave length, and can only exist with free BC because they have a nonzero displacement at the surfaces. Rayleigh waves have both a nonzero curl and nonzero divergence; therefore, they cannot be described by a scalar wave equation. *Neither elastic waves with fixed BCs nor scalar waves with any BC can support Rayleigh waves.*

## III. NUMERICAL METHOD

### A. The finite-difference time-domain (FDTD) method for the elastic and scalar wave equation

We solve the elastic (3) and scalar (5) wave equations in our structures using the finite-difference time-domain method, which is an efficient technique that discretizes

the wave equation in both space and time by replacing the partial derivatives with finite differences. While the FDTD method is best known for solving the electromagnetic wave equation [53, 54], the method has been used with many wave equations, such as the Schrödinger [55, 56], Klein-Gordon [55], scalar [57], and elastic wave equations [58, 59]. Elastic-medium FDTD has been used to investigate transmission through superlattices [29] and phononic materials [60–62], but it had not been used before to calculate thermal conductivity.

Unlike many methods used to investigate elastic materials, elastic-medium FDTD is not limited to weak roughness or to any specific geometry. The technique is computationally simple and fast; the core of the simulation requires only a few lines of element-wise array operations, which can be computed quickly on modern processors.

We use graphenelike Lamé parameters from [63]:  $\lambda = 32.0 \text{ J/m}^2$  and  $\mu = 160.2 \text{ J/m}^2$ . (Equivalently,  $c_l = 2.14 \times 10^4 \text{ m/s}$  and  $c_t = 1.44 \times 10^4 \text{ m/s}$ .) We choose the grid-cell size (GCS), denoted  $h$ , to be the graphene lattice constant ( $h=0.246 \text{ nm}$ ), which means that the shortest wavelength in our system will be similar to that in graphene. We use the GCS  $h$  as a unit of length in this paper. Our choice of material parameters and  $h$  sets the stability condition for the simulation time step  $\Delta t < h/c_l\sqrt{2}$  [59]. We chose  $\Delta t = 0.95 \text{ fs}$ , one tenth of the maximum allowed value. Our time step is comparable to the 0.1-0.5 fs often used in graphene MD simulations [4, 15, 64–66]. We simulate 100-GCS-wide (24.6 nm) nanoribbons with random surface roughness that has a Gaussian autocorrelation function  $C_g(x) = \Delta^2 e^{-x^2/\xi^2}$ , where  $\Delta$  and  $\xi$  are the RMS roughness and correlation length, respectively [67].

While the elastic wave equation (3) can be directly solved with the FDTD method to obtain  $\mathbf{u}$  [58], we instead use the velocity-stress formulation [59] because it allows for a simple and stable implementation of free BCs and because the velocity and stress are ultimately what we need to find  $\mathbf{J}$ .

Taking the time derivatives of the strain equation (1a), Hooke’s law (1b), and elastic wave equation (3) while defining  $\mathbf{v} = \dot{\mathbf{u}}$  yields:

$$\dot{\sigma}_{ij} = \frac{1}{2} (\partial_j \dot{v}_i + \partial_i \dot{v}_j), \quad (7a)$$

$$\dot{\tau}_{ij} = \lambda \dot{\sigma}_{ll} \delta_{ij} + 2\mu \dot{\sigma}_{ij}, \quad (7b)$$

$$\rho \dot{\mathbf{v}} = \nabla \cdot \dot{\boldsymbol{\tau}}. \quad (7c)$$

The elastic wave equation is thus broken into two first order differential equations. [Although there are three equations above,  $\dot{\sigma}$  and  $\dot{\tau}$  are linearly related via Hooke’s law (1b).] The stress-strain formulation [59] solves for the stress-strain and velocity using a leapfrog technique on a staggered, square grid (See Fig. 2). We found that the second-order-accurate [59] and fourth-order-accurate [68] spatial finite difference operators were both stable and suitable for our purposes. We used the second-order-accurate operator because it is computationally simpler.

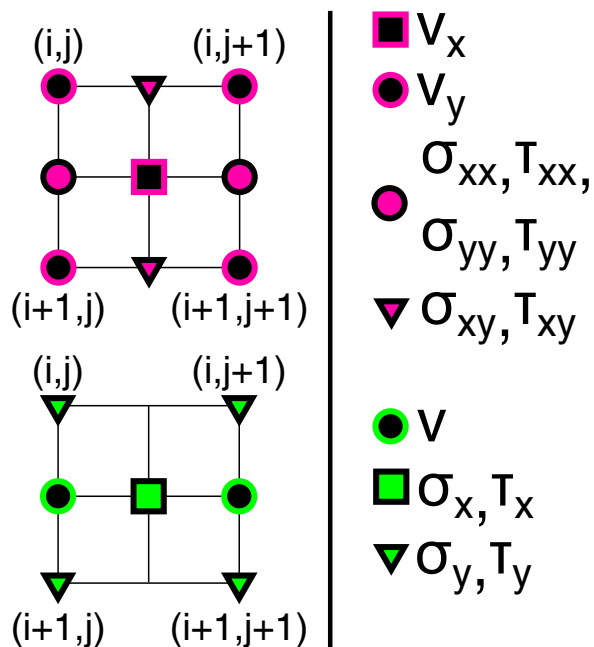


FIG. 2. (Color online) The staggered grid used for the FDTD solution to the elastic (top) and scalar (bottom) wave equations.  $(i, j)$  enumerate the grid cells along the  $x$  and  $y$  directions. The symbols (squares, triangles, and circles) show where on the grid the different components of  $\mathbf{v}$ ,  $\sigma$ , and  $\tau$  are defined.

To implement free boundaries, we used the “vacuum formalism,” where materials parameters  $\mu$ ,  $\lambda$ , and  $\rho^{-1}$  are set to zero outside the structure. For accuracy and stability, a half-grid-cell-thick fictitious layer of material is added around the structure to ease the transition from the material to vacuum [68]. Fixed BCs are simpler to implement: we force  $\mathbf{v} = 0$  on the surface.

The 2D scalar wave equation can be recovered by taking the 3D elastic wave equation and setting  $\partial_z v_z = 0$ . To keep our elastic and scalar FDTD methods consistent, we take the 3D generalization of our elastic wave FDTD technique [69] and set  $\partial_z v_z = 0$  to create our 2D scalar wave equation FDTD method. (The method can also be derived directly [57].) Free and fixed BCs are enforced by setting the stress or velocity, respectively, to zero on the surface.

Because we simulate a linear elastic material, our model does not include phonon-phonon scattering, which would imply a nonlinear restoring force in the wave equation [25]. Our simulation is suitable for investigating structures where surface or boundary roughness is the dominant scattering mechanism.

### 1. Energy conservation in long simulations

The elastic wave FDTD technique was originally developed to model earthquakes [58, 70]. Many commonly used free-surface implementations are known to have

long-term instabilities [71]; however, these instabilities are not an issue for typical seismic simulations, which are often short and have absorbing boundary conditions along some domain edges. In contrast, our simulations require stability and energy conservation even for very long simulations (millions of time steps). We tried several different combinations of FDTD grids, finite difference operators, and free BCs before we found a working combination that conserves energy even for very long simulations. To our knowledge, it had not been previously reported that the combination of BCs and FDTD method we report is energy-stable.

### 2. Dispersion and anisotropy

Discretizing wave equations introduces some dispersion and anisotropy to the dispersion relations, which are generally undesirable for modeling continuum materials. However, as we ultimately care about phonons in atomic materials, which also have dispersion and anisotropy, discretization can actually bring the elastic medium model closer to an atomic model. We also note that it is possible to deliberately add anisotropy to elastic-material FDTD simulations at the cost of additional complexity [72, 73].

### 3. FDTD vs. Molecular Dynamics

Because of the discretization, our FDTD model has similarities to a molecular dynamics (MD) simulation, with springlike nearest-neighbor potentials and with the discretized material elements playing a similar role to atoms in MD. The primary advantages of an FDTD simulation over an MD simulation are simplicity, scalability, and computational speed. We can simulate relatively large structures with significantly less computational cost than an MD simulation. The trade-off is that the FDTD method cannot accurately account for the short-wavelength limit or anharmonic potentials of atomic materials. The harmonic potentials and classical statistics also mean that our thermal conductivity is independent of temperature.

## B. Thermal conductivity calculation

We compute the thermal conductivity in a similar way to an equilibrium molecular dynamics simulation [37, 38]. First, we initialize all the discretized elements with a random velocity drawn from a Maxwell-Boltzmann distribution. The simulation can become unstable if the net momentum is too far from zero. Because we draw a finite number of samples from the Maxwell-Boltzmann distribution, the net momentum will be small but nonzero. To account for this, before starting the simulation we adjust the velocities so that the structure has zero net momentum. We likewise adjust the velocities so that the kinetic

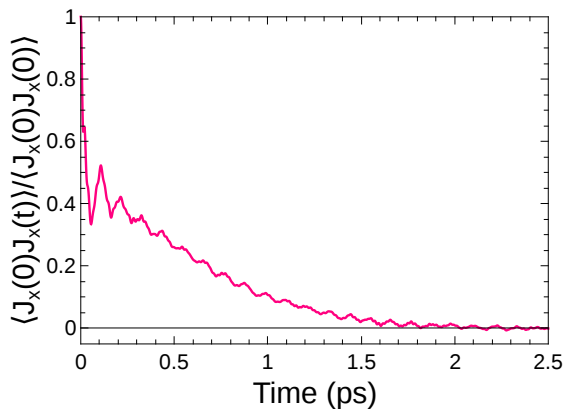


FIG. 3. (Color online) Representative heat current autocorrelation function versus time. The curve is similar to those obtained for equilibrium molecular dynamics simulations [38].

energy is equally divided between the  $x$  and  $y$  motion,  $x$  being along the nanoribbon.

We run the simulation for 100,000 time steps to let the system equilibrate. Then, the simulation runs an additional 900,000 time steps in the steady state. At each time step, we calculate the net  $\mathbf{J}$ , Eq. (2). Finally, we calculate the thermal conductivity  $\kappa$  using the Green-Kubo formula:

$$\kappa = \frac{1}{k_B T^2 \Omega} \int_0^\infty \langle J_x(0) J_x(t) \rangle dt, \quad (8)$$

where  $T$  is the system temperature,  $\Omega$  is the system volume, and the  $x$ -axis is along the ribbon. We directly compute the integral and cut it off after the first dip, when  $\langle J_x(0) J_x(t) \rangle$  first reaches zero [38]. Figure 3 shows that the current-current correlation function obtained via FDTD has a temporal dependence similar to that obtained in MD simulations, underscoring the similarity between the two techniques.

#### IV. SURFACE SCATTERING AND MODE CONVERSION

The longitudinal and transverse phonon modes can be decoupled inside a structure, but they generally have to be coupled at the surface in order to satisfy physical boundary conditions. For example, the fixed BC for the elastic wave equation ( $\mathbf{u} = 0$ ) combined with Eq. (4) requires  $\nabla\phi = -\nabla \times \Psi$ , which clearly couples the scalar and vector potentials,  $\phi$  and  $\Psi$ , along with their corresponding modes. Applying fixed boundary conditions separately to the decoupled scalar wave equations ( $\phi = 0$  and  $\Psi = 0$ ) *does not couple the two modes* and is not equivalent to the boundary condition for the elastic wave equation. In short, the elastic wave equation allows for mode conversion, while the decoupled scalar wave equations do not.

Figure 4 illustrates mode conversion at the surface via a colorized energy-density profile for a simple example: a longitudinal wave packet incident upon a smooth, free surface at the top. The longitudinal wave is reflected into longitudinal and transverse waves; there is no conversion from bulk into Rayleigh waves at a smooth surface [5, 10–12]. Wei *et al.* [4] obtained similar results based on a molecular-dynamics simulation of mode conversion between bulk modes at smooth graphene surfaces. There are many fine points of conversion between bulk modes, such as the angles where the incoming longitudinal wave is converted entirely into a reflected transverse wave (right panel in Fig. 4). However, in Sec. V we will show that mode conversion between bulk modes has little impact on phonon thermal transport in our nanoribbonlike systems and we therefore focus on conversion between bulk modes and Rayleigh waves at rough surfaces.

Figure 5 shows a snapshot of the spatial energy density, represented by color, of a Rayleigh wave packet that moves from left to right along the bottom surface. The packet arrived from a region near a smooth surface (bottom left) and impinged upon a rougher region (bottom right); the snapshot was taken shortly thereafter. The packet remained largely intact, albeit slightly distorted, as it continued to travel along the rough surface. Some energy is radiated into bulk modes, but the amount is small compared to the amount of energy still in the packet (note that the energy density is plotted on a log scale). This finding is in line with previous studies of Rayleigh-wave scattering from disordered surfaces, which found that Rayleigh waves are tolerant of disorder on scales smaller than the wavelength [11, 12].

Figure 6 shows examples of mode conversion for an incident longitudinal wave packet scattering from surfaces with different roughness (nearly smooth: left column, very rough: right column) and boundary conditions (free BC: top row; fixed BC: bottom row). Each panel shows the spatial energy density, represented by color and on the long scale. The incoming wave profile is the same as in Fig. 4, and is omitted here for clarity; the color represents only the energy density for the outgoing wave packets. First, the specularly scattered bulk modes are visible, albeit distorted, for the nearly smooth surfaces of both BCs. In contrast, scattering from the very rough surfaces of both BC is very diffuse. Second, no energy remains localized at the fixed surfaces, because fixed surfaces do not support surface modes. In contrast, a significant amount of energy is captured near the free surfaces. The longitudinal wave incident on the nearly smooth free surface is partially converted into Rayleigh waves. One Rayleigh-wave energy-density profile has been enlarged in the inset to the top left panel.

For the very rough free surface (Fig. 6, top right panel), the energy remaining near the surface is concentrated in a few places and has not propagated nearly as far along the surface as it did in case of its nearly smooth counterpart. The concentrated energy is similar to the spatially localized modes (SLMs) seen in molec-

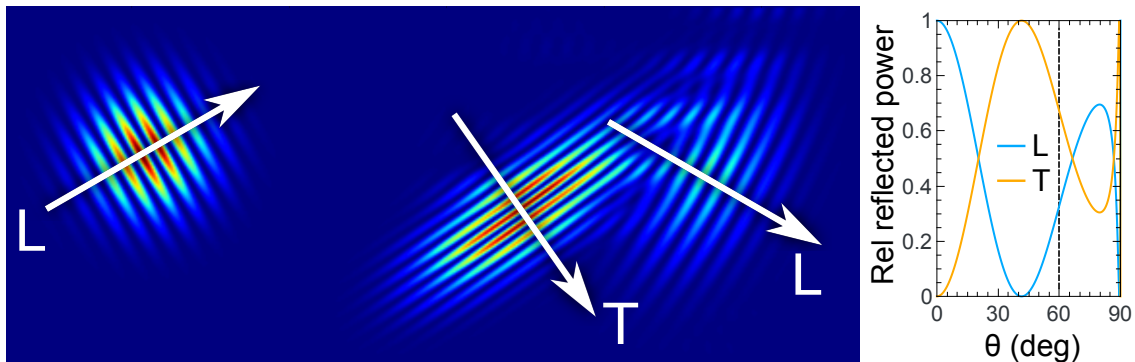


FIG. 4. (Color online) (Left panel) Visualization of elastic wave mode conversion at a smooth surface. Color represents the spatial profile of the energy density (log scale, arbitrary units; red–high, blue–low). A longitudinal wave packed is incident on a free, smooth top surface at  $60^\circ$  from the surface normal. One longitudinal and one transverse wave packet are reflected. The transverse wave can be identified by its shorter wavelength and slower group velocity. The plot to the right shows the relative energy in the scattered wave packets as a function of the angle of incidence. The plot was made for the graphenelike material parameters described later in the paper. The material parameters have a strong effect on the angular dependence seen in the plot.

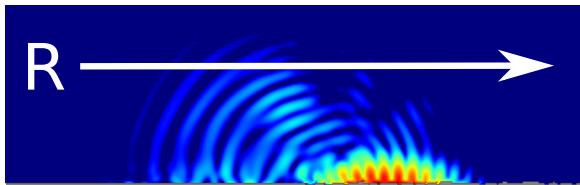


FIG. 5. (Color online) Snapshot of a Rayleigh wave that scattered from a rough surface. Color represents the energy-density profile (log scale, arbitrary units; red–high, blue–low). A Rayleigh wave packet was launched from left to right, moving first along a smooth bottom surface (left) and then along a rough bottom surface (right). Once the packet reaches the roughness (snapshot was taken shortly thereafter), it starts radiating energy into bulk modes. However, the conversion from Rayleigh into bulk modes is relatively weak. The energy leaves the packet slowly, and the packet continues to the right with little distortion.

ular dynamics simulations by Kang and Estreicher [26]. In particular, the surface modes we see are similar to the “wag modes” predicted for atoms terminating bonds on nanowires [26, 74]. Instead of a terminating atom, a protuberance of the nanoribbon wags back and forth. (See Fig. 7.) SLMs were found to release their energy over relatively long time scales, and neighboring SLMs are often weakly coupled, so energy travels very slowly along the surface. Although the energy at the very rough free surface has effectively become localized and is no longer a propagating wave, for consistency, we will still refer to the localized surface modes as Rayleigh waves.

## V. THERMAL CONDUCTIVITY AND RAYLEIGH WAVES

We now turn to the thermal conductivity of nanoribbons of width 24.6 nm; this width equals 100 times the grid-cell size  $h = 0.246$  nm. The results, summarized in Table I, are the averages from 100,000 simulations. For each ribbon, we simulate the elastic wave equation and the two decoupled scalar equations. The thermal conductivities given for the scalar waves are the sum of the thermal conductivities of the two decoupled scalar waves. The results follow the general pattern seen elsewhere [19, 20] of  $\kappa$  decreasing with increasing rms roughness  $\Delta$  and decreasing correlation length  $\xi$ , with  $\xi$  having a weaker effect than  $\Delta$ .

Because  $\kappa$  depends weakly on  $\xi$ , we simplify the analysis by focusing on  $\Delta$ . Figure 8 shows  $\kappa$  as a function of  $\Delta$  for  $\xi = 9h$ . Scalar waves (with both BCs) and elastic waves with fixed surfaces have very similar results, which converge at large  $\Delta$ . Elastic waves with free BCs have significantly lower thermal conductivities.

It may seem surprising that the scalar and fixed elastic results are nearly identical, but the results are in line with one of Casimir’s insights [75]: for bulk modes scattering from reflective surfaces, sufficient roughness scatters everything diffusely; the surface behaves like a blackbody that absorbs all incident phonons and immediately radiates them away at random angles. The details of the diffuse scattering (fixed or free surface, mode conversion or not) are irrelevant. All that matters is that the surface reflects everything diffusely. In this way, Casimir avoided the issue of mode conversion, even though he considered elastic waves. In Fig. 8, we see similar results. When the roughness is low, there are some differences between the scalar and fixed elastic results, but the results all converge as the roughness increases and the scattering becomes totally diffuse.

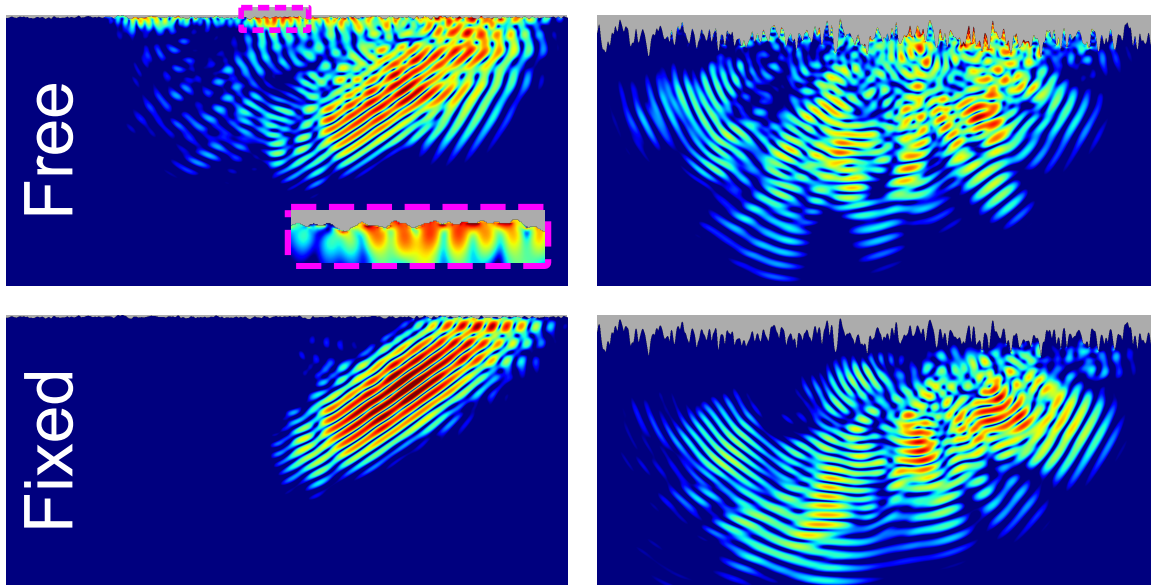


FIG. 6. (Color online) Snapshots of bulk elastic waves scattered from rough surfaces (top of each panel). Color represents the energy-density profile (log scale, arbitrary units; red–high, blue–low). A longitudinal wave packet was incident on a surface that is nearly smooth and free (top left panel), very rough and free (top right), nearly smooth and fixed (bottom left), and very rough and fixed (bottom right). Surface Rayleigh modes are visible only for the free surfaces (i.e., energy is localized near the free surfaces), because fixed surfaces do not support surface modes. (Inset to top left panel) Zoom-in on the energy-density profile for a free, nearly smooth surface (region inside the dashed box on the main panel) reveals a wave packet localized near the surface: a Rayleigh mode. (Compare with the Rayleigh wave packet in Figure 5.)

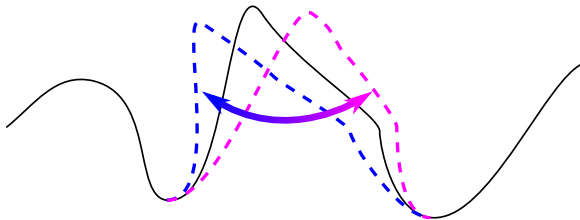


FIG. 7. (Color online) Exaggerated illustration of a “wag mode”. The black line is the edge of a rough nanoribbon, and the protuberance can wag back and forth. Of the waves we consider, only elastic waves with free BCs can support wag modes.

However, Casimir’s insight only holds for reflective surfaces. Rayleigh waves allow surfaces to capture incident energy instead of reflecting it. Additionally, Casimir only considered planar surfaces, which puts a lower limit on the thermal conductivity obtained. The limitations to Casimir’s assumptions explain why the free elastic results are different from the others, but not why they are necessarily lower. At first glance, it might seem that Rayleigh waves should increase thermal conductivity; after all, Rayleigh waves are another mode to transport energy, and they also have the benefit of always traveling down the axis of the ribbon. However, Rayleigh waves have the disadvantage of being slower than either transverse or longitudinal waves, even when there is no disorder. More importantly, Rayleigh waves concentrate the

TABLE I. Calculated thermal conductivity (in  $\text{W}/\text{m} \cdot \text{K}$ ) of a 24.6-nm-wide graphenelike nanoribbon calculated based on the FDTD solution to the elastic and scalar wave equations with free and fixed boundary conditions. Roughness rms value  $\Delta$  and correlation length  $\xi$  are measured in units of grid-cell size  $h$  ( $h=0.246$  nm).

$\xi \rightarrow$	1	2	3	4	5	1	2	3	4	5
$\Delta \downarrow$	Elastic waves, free BCs					Scalar waves, free BCs				
3	1254	752	540	426	343	2916	1351	782	516	371
6	1409	757	563	426	340	3093	1361	794	560	393
9	1479	814	588	431	353	3210	1455	820	567	414
12	1620	834	580	455	362	3544	1499	882	582	427
15	1695	898	591	458	365	3727	1581	874	610	431
	Elastic waves, fixed BCs					Scalar waves, fixed BCs				
3	2309	1172	754	529	396	3457	1411	842	564	417
6	2697	1267	750	573	399	3530	1520	853	541	433
9	2934	1255	812	556	423	4289	1673	917	579	434
12	3272	1382	810	581	424	4063	1746	955	600	434
15	3287	1531	867	585	450	4535	1812	1020	645	460

energy where there is the most disorder, at the surface; Rayleigh waves readily become localized due to disorder, so the energy trapped in them contributes little to thermal transport.

The effect of Rayleigh-wave localization due to disorder is visible in Fig. 9, which depicts the difference be-

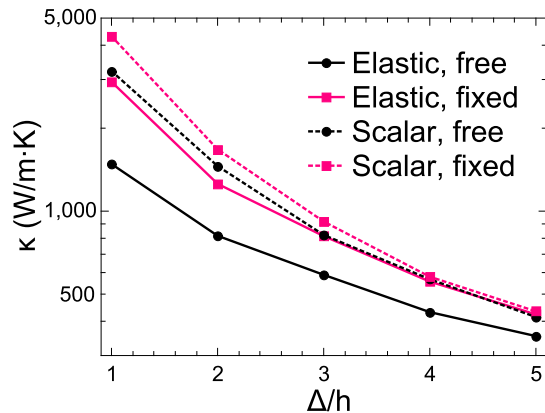


FIG. 8. (Color online) Thermal conductivity  $\kappa$  of a nanoribbon as a function of rms roughness  $\Delta$  (given in the units of  $h$ , the grid-cell size), as obtained based on the FDTD solution to elastic (solid lines) and scalar (dashed lines) wave equations with free (black circles) and fixed (red squares) boundary conditions. The correlation length  $\xi$  is fixed at  $9h$  and the nanoribbon width is  $100h$  ( $h = 0.246$  nm).

tween the energy-density profiles across the ribbon for free BC (Rayleigh waves present) and fixed boundary conditions (Rayleigh waves absent), normalized with the average energy density. Each curve is obtained by averaging over the length. Distance from the axis is in the units of nanoribbon width, so the average width goes from  $-1/2$  to  $1/2$ . Stars denote the minimal and squares the maximal distance between an edge and ribbon axis; in other words, the star-to-star distance denotes the minimum width (we can consider this the bulk region), while the square-to-square distance is the maximal ribbon width. We note that, with high disorder, there is less energy density in the middle for ribbons that support Rayleigh waves, which means that more energy from the middle is lost to the surface states; in the presence of disorder the energy effectively shifts away from the bulk and becomes trapped in the surface Rayleigh modes. Consequently, a ribbon with a free surface has noticeably more energy density in the rough region near the edges (for distances between the star and the square) when the rms roughness is pronounced.

As an aside, we also simulated 45-nm-wide graphene nanoribbons with 0.6-nm rms roughness, similar to those measured by Bae *et al.* [76]. Our calculation, which only accounts for edge roughness, yielded  $\kappa$  of around  $500$  W/m·K; Bae *et al.* measured  $\kappa \approx 80$  W/m·K at 300 K, considerably lower because of three-phonon scattering. Other simulation techniques have also predicted high thermal conductivities for rough graphene nanoribbons that are smaller than the approximately 25-nm-wide nanoribbons we consider here [15–17]. For example, Evans *et al.* [15] predicted a thermal conductivity of  $\approx 3000 - 4000$  W/m·K for a 11-nm-wide graphene nanoribbon with one lattice constant of rms edge roughness.

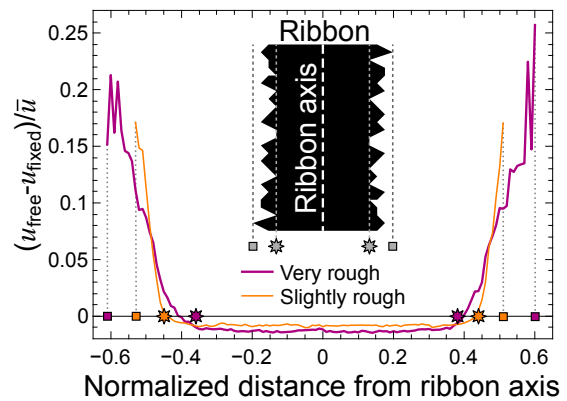


FIG. 9. (Color online) Difference in the energy densities for identical nanoribbons with free boundaries (supporting Rayleigh waves) and fixed boundaries (no surface waves) versus position with respect to the ribbon axis. The position is given in the units of nanoribbon width and the energy-density difference is normalized to the average value. The energy-density-difference profiles are presented for two different relative rms roughnesses in the units of nanoribbon width,  $\Delta/W$  (orange curve) and  $\Delta/W = 0.02$  and  $\Delta/W = 0.05$  (purple curve). Because of roughness, the distance of the edge from the nanoribbon axis varies; stars denote the minimal while squares denote the maximal distance of the edge from the axis; the star-to-star region can be considered the nanoribbon bulk. The free-minus-fixed energy-density profile represents the energy redistribution that stems from the presence of Rayleigh surface waves. It is notable that the energy gets moved away from the bulk and into the Rayleigh surface waves, an effect that becomes more pronounced with increasing roughness. At high roughness, the energy density associated with Rayleigh waves can become quite pronounced.

## VI. CONCLUSION

Our results have implications for methods and models used to simplify phonon-surface scattering. Simplified phonon-surface scattering models are particularly important for many modern nanostructures, which are often too large to simulate with first-principles methods [14].

Many phonon-surface scattering models use the phenomenological concept of a specular parameter [10, 23–25, 77, 78], the probability a wave will scatter specularly from a rough surface. Existing specular parameter models are tied to the scalar wave model, which does not support mode conversion. Indeed, Ziman adapted the concept of a specular parameter from electromagnetic waves, which do not undergo meaningful mode conversion [24]. Our results underscore the importance of the ongoing work to extend the specular parameter model to account for mode conversion [79] and Rayleigh waves [10]. However, even with improvements, the specular parameter concept only makes sense in the limit of weak roughness; all specular parameter models have a “Casimir limit” when the specular parameter is zero and all scattering is diffuse [20], yet in many nanostructures thermal conductivities far below that limit have



been measured [18, 19, 80].

Another tool used to study phonon transport in relatively large nanostructures is phonon Monte Carlo (PMC), where a large ensemble of phonons are treated as point particles that drift and scatter [20, 67, 81–84]. Current PMC simulations do not allow for mode conversion or Rayleigh waves. Instead, PMC simulations either have phonons scatter specularly at the surface [20, 67, 80, 83] or have a specular parameter with the reflected phonon of the same mode as the incident phonon [20, 84]. Monte Carlo simulations for chaotic ray-splitting billiards are similar to PMC simulations, and the chaotic ray-splitting billiard simulations have been extended to allow for mode conversion between bulk modes [85]. The technique could be extended to PMC and, in principle, could support Rayleigh waves if the scattering amplitudes between bulk and Rayleigh waves are known and if Rayleigh-wave localization is taken into account.

Finally, let us consider what our results mean for the many phonon-surface scattering models based on scalar waves [40–51]. While the scalar wave equation significantly overestimates  $\kappa$ , it does produce qualitatively similar results to the elastic wave equation:  $\kappa$  decreases with increasing  $\Delta$  and with decreasing  $\xi$ . Problems arise when accurate predictions are needed for known surface roughness. This issue was seen in the work of Santamore and Cross, who studied a system first using scalar [41] and then elastic wave equations [33]. While both models could fit experimental data, they required significantly

different surface roughness parameters, and it was hard to judge which fitting parameters were correct because the actual surface roughness features were unknown. For a surface with a well-characterized roughness profile, one could expect that the calculated  $\kappa$  might be inaccurate if the scalar wave model is inappropriately used when significant mode conversion takes place.

We have shown that Rayleigh waves play an important role in phonon-surface scattering, yet they are not included in most phonon-surface scattering models. However, both surface and internal scattering mechanisms (phonon-phonon, mass-difference, etc.) play important roles in nanoscale thermal transport. Additional work is needed to develop models that include internal scattering mechanisms, incorporate Rayleigh waves and surface mode conversion, and are able to simulate large nanostructures.

## ACKNOWLEDGMENTS

The authors gratefully acknowledge support by the U.S. Department of Energy, Office of Basic Energy Sciences, Division of Materials Sciences and Engineering under Award DE-SC0008712. This work was performed using the compute resources and assistance of the UW-Madison Center for High Throughput Computing (CHTC) in the Department of Computer Sciences.

- 
- [1] L. Landau and E. Lifshitz, *Theory of Elasticity* (Pergamon Press, 1986).
- [2] G. A. Northrop and J. P. Wolfe, Phys. Rev. Lett. **52**, 2156 (1984).
- [3] T. Nakayama, Phys. Rev. B **32**, 777 (1985).
- [4] Z. Wei, Y. Chen, and C. Dames, J. Appl. Phys. **112**, 024328 (2012).
- [5] J. P. Wolfe, *Imaging Phonons* (Cambridge University Press, 1998).
- [6] L. Rayleigh, P. Lond. Math. Soc. **s1-17**, 4 (1885).
- [7] R. Wallis, Prog. Surf. Sci. **4**, 233 (1974).
- [8] R. Wallis, Surf. Sci. **299-300**, 612 (1994).
- [9] E. Urazakov and L. Fal'kovskii, JETP **36**, 1214 (1973).
- [10] A. A. Maznev, Phys. Rev. B **91**, 134306 (2015).
- [11] R. G. Steg and P. G. Klemens, Phys. Rev. Lett. **24**, 381 (1970).
- [12] T. Sakuma, Phys. Rev. B **8**, 1433 (1973).
- [13] B. Garber, M. Cahay, and G. E. W. Bauer, Phys. Rev. B **62**, 12831 (2000).
- [14] D. G. Cahill, P. V. Braun, G. Chen, D. R. Clarke, S. Fan, K. E. Goodson, P. Keblinski, W. P. King, G. D. Mahan, A. Majumdar, H. J. Maris, S. R. Phillpot, E. Pop, and L. Shi, Applied Physics Reviews **1**, 011305 (2014).
- [15] W. J. Evans, L. Hu, and P. Keblinski, Appl. Phys. Lett. **96**, 203112 (2010).
- [16] H. Sevinçli and G. Cuniberti, Phys. Rev. B **81**, 113401 (2010).
- [17] W. Li, H. Sevinçli, G. Cuniberti, and S. Roche, Phys. Rev. B **82**, 041410 (2010).
- [18] A. I. Hochbaum, R. Chen, R. D. Delgado, W. Liang, E. C. Garnett, M. Najarian, A. Majumdar, and P. Yang, Nature **451**, 163 (2008).
- [19] J. Lim, K. Hippalgaonkar, S. C. Andrews, A. Majumdar, and P. Yang, Nano Lett. **12**, 2475 (2012).
- [20] L. N. Maurer, Z. Aksamija, E. B. Ramayya, A. H. Davoody, and I. Knezevic, Appl. Phys. Lett. **106**, 133108 (2015).
- [21] A. A. Maradudin, in *Physics of Phonons*, Lecture Notes in Physics, Vol. 285, edited by T. Paszkiewicz (Springer Berlin Heidelberg, 1987) pp. 82–147.
- [22] A. A. Maradudin, in *Nonequilibrium Phonon Dynamics*, NATO ASI Series, Vol. 124, edited by W. Bron (Springer US, 1985) pp. 395–599.
- [23] R. Berman, F. E. Simon, and J. M. Ziman, Proc. R. Soc. A **220**, 171 (1953).
- [24] R. Berman, E. L. Foster, and J. M. Ziman, Proc. R. Soc. A **231**, 130 (1955).
- [25] J. M. Ziman, *Electrons and Phonons: the Theory of Transport Phenomena in Solids* (Clarendon Press, 1960).
- [26] B. Kang and S. K. Estreicher, Phys. Rev. B **89**, 155409 (2014).
- [27] D. C. Hurley, S. Tamura, J. P. Wolfe, and H. Morkog, Phys. Rev. Lett. **58**, 2446 (1987).
- [28] H. Kato, H. J. Maris, and S.-i. Tamura, Phys. Rev. B **53**, 7884 (1996).
- [29] H. Kato and S.-i. Tamura, J. Phys. Condens. Matter **9**,

- 6791 (1997).
- [30] S. Mizuno, Phys. Rev. B **68**, 193305 (2003).
- [31] N. W. Ashcroft and D. N. Mermin, *Solid State Physics* (Thomson Learning, 1976).
- [32] Y. Tanaka, F. Yoshida, and S. Tamura, Phys. Status Solidi C **1**, 2625 (2004).
- [33] D. H. Santamore and M. C. Cross, Phys. Rev. Lett. **87**, 115502 (2001).
- [34] W.-X. Li, K.-Q. Chen, W. Duan, J. Wu, and B.-L. Gu, J. Phys. Condens. Matter **16**, 5049 (2004).
- [35] J. Hyun Oh, M. Shin, and M.-G. Jang, J. Appl. Phys. **111**, 044304 (2012), 10.1063/1.3684973.
- [36] J. Hyun Oh, M.-G. Jang, M. Shin, and S.-H. Lee, Applied Physics Letters **100**, 113110 (2012).
- [37] A. J. C. Ladd, B. Moran, and W. G. Hoover, Phys. Rev. B **34**, 5058 (1986).
- [38] J. Li, L. Porter, and S. Yip, J. Nucl. Mater. **255**, 139 (1998).
- [39] R. Snieder, in *Scattering*, edited by P. Sabatier and R. Pike (Academic Press, London, 2002) pp. 528 – 542.
- [40] A. Kambili, G. Fagas, V. I. Fal'ko, and C. J. Lambert, Phys. Rev. B **60**, 15593 (1999).
- [41] D. H. Santamore and M. C. Cross, Phys. Rev. B **63**, 184306 (2001).
- [42] M. C. Cross and R. Lifshitz, Phys. Rev. B **64**, 085324 (2001).
- [43] A. N. Cleland, D. R. Schmidt, and C. S. Yung, Phys. Rev. B **64**, 172301 (2001).
- [44] X. F. Wang, M. S. Kushwaha, and P. Vasilopoulos, Phys. Rev. B **65**, 035107 (2001).
- [45] S.-X. Qu and M. R. Geller, Phys. Rev. B **70**, 085414 (2004).
- [46] L. Wen-Xia, L. Tian-Yu, and L. Chang-Long, Chinese Phys. Lett. **23**, 2522 (2006).
- [47] W. Li and K. Chen, Phys. Lett. A **357**, 378 (2006).
- [48] L.-M. Tang, L. Wang, W.-Q. Huang, B. S. Zou, and K.-Q. Chen, J. Phys. D: Appl. Phys. **40**, 1497 (2007).
- [49] H.-Y. Zhang, H.-J. Li, W.-Q. Huang, and S.-X. Xie, J. Phys. D: Appl. Phys. **40**, 6105 (2007).
- [50] Y. Wang, L.-L. Wang, L.-M. Tang, B. Zou, and L.-H. Zhao, J. Phys. D: Appl. Phys. **40**, 7159 (2007).
- [51] G. B. Akguc and J. Gong, Phys. Rev. B **80**, 195408 (2009).
- [52] Y. Tanaka, F. Yoshida, and S. Tamura, Phys. Rev. B **71**, 205308 (2005).
- [53] K. Yee, IEEE T. Antenn. Propag. **14**, 302 (1966).
- [54] A. Taflove and S. C. Hagness, *Computational Electrodynamics: The Finite-Difference Time-Domain Method* (Artech House, 2005).
- [55] H. F. Harmuth, Journal of Mathematics and Physics **36**, 269 (1957).
- [56] D. M. Sullivan and P. M. Wilson, J. Appl. Phys. **112**, 064325 (2012), 10.1063/1.4754812.
- [57] J. Virieux, Geophysics **49**, 1933 (1984).
- [58] Z. Alterman and F. C. Karal, Bull. Seismol. Soc. Am. **58**, 367 (1968).
- [59] J. Virieux, Geophysics **51**, 889 (1986).
- [60] M. M. Sigalas and N. García, J. Appl. Phys. **87**, 3122 (2000).
- [61] D. Garcia-Pablos, M. Sigalas, F. R. Montero de Espinosa, M. Torres, M. Kafesaki, and N. García, Phys. Rev. Lett. **84**, 4349 (2000).
- [62] J. O. Vasseur, P. A. Deymier, B. Chenni, B. Djafari-Rouhani, L. Dobrzynski, and D. Prevost, Phys. Rev. Lett. **86**, 3012 (2001).
- [63] K. V. Zakharchenko, M. I. Katsnelson, and A. Fasolino, Phys. Rev. Lett. **102**, 046808 (2009).
- [64] J.-W. Jiang, J.-S. Wang, and B. Li, Phys. Rev. B **80**, 113405 (2009).
- [65] Z. Guo, D. Zhang, and X.-G. Gong, Appl. Phys. Lett. **95**, 163103 (2009).
- [66] J. Hu, X. Ruan, and Y. P. Chen, Nano Lett. **9**, 2730 (2009), pMID: 19499898.
- [67] E. B. Ramayya, L. N. Maurer, A. H. Davoody, and I. Knezevic, Phys. Rev. B **86**, 115328 (2012).
- [68] C. Zeng, J. Xia, R. D. Miller, and G. P. Tsoufias, Geophysics **77**, T1 (2012).
- [69] R. W. Graves, Bull. Seismol. Soc. Am. **86**, 1091 (1996).
- [70] K. R. Kelly, R. W. Ward, S. Treitel, and R. M. Alford, Geophysics **41**, 2 (1976).
- [71] R. Stacey, Bull. Seismol. Soc. Am. **84**, 171 (1994).
- [72] H. Igel, P. Mora, and B. Rioulet, Geophysics **60**, 1203 (1995).
- [73] M. Sato, Jpn. J. Appl. Phys. **47**, 3931 (2008).
- [74] S. K. Estreicher, T. M. Gibbons, and M. B. Bebek, J. Appl. Phys. **117**, 112801 (2015), 10.1063/1.4913826.
- [75] H. Casimir, Physica **5**, 495 (1938).
- [76] M.-H. Bae, Z. Li, Z. Aksamija, P. N. Martin, F. Xiong, Z.-Y. Ong, I. Knezevic, and E. Pop, Nat. Commun. **4**, 1734 (2012).
- [77] S. B. Soffer, J. of Appl. Phys. **38**, 1710 (1967).
- [78] J. E. Graebner, M. E. Reiss, L. Seibles, T. M. Hartnett, R. P. Miller, and C. J. Robinson, Phys. Rev. B **50**, 3702 (1994).
- [79] J. A. Ogilvy, NDT International **19**, 371 (1986).
- [80] C. Blanc, A. Rajabpour, S. Volz, T. Fournier, and O. Bourgeois, Applied Physics Letters **103**, 043109 (2013).
- [81] R. B. Peterson, J. Heat Transfer **116**, 815 (1994).
- [82] D. Lacroix, K. Joulain, and D. Lemonnier, Phys. Rev. B **72**, 064305 (2005).
- [83] J. Randrianalisoa and D. Baillis, J. Heat Transfer **130**, 072404 (2008).
- [84] A. Mittal and S. Mazumder, J. Heat Transfer **132**, 052402 (2010).
- [85] L. Couchman, E. Ott, and T. M. Antonsen, Phys. Rev. A **46**, 6193 (1992).